Journal of Power Sources 195 (2010) 3017–3024

Contents lists available at ScienceDirect

Journal of Power Sources

journal homepage: www.elsevier.com/locate/jpowsour

Asymmetric capacitor based on superior porous Ni–Zn–Co oxide/hydroxide and carbon electrodes

Huanlei Wang, Qiuming Gao*, Juan Hu

State Key Laboratory of High Performance Ceramics and Superfine Microstructures, Graduate School, Shanghai Institute of Ceramics, Chinese Academy of Sciences, 1295 Dingxi Road, Shanghai 200050, People's Republic of China

ARTICLE INFO

Article history:
Received 30 September 2009
Accepted 13 November 2009
Available online 18 November 2009

Keywords:
Porous oxide/hydroxide
Porous carbon
Metal-organic framework
Asymmetric capacitor
Electrochemical performance

ABSTRACT

Hierarchical porous multi-phase Ni–Zn–Co oxide/hydroxide is synthesized by using metal-organic framework-5 (MOF-5) as the template. Hierarchical porous carbon is obtained by the facile direct decomposition of the MOF-5 framework with phenolic resin. The structures and textures are characterized by X-ray diffraction, high-resolution transmission electron microscopy, scanning electron microscopy, and nitrogen sorption at 77 K. An asymmetric capacitor incorporating the Ni–Zn–Co oxide/hydroxide as the positive electrode and the porous carbon as the negative electrode is fabricated. A maximum energy density of 41.65 Wh kg^{-1} is obtained, which outperforms many other available asymmetric capacitors. The asymmetric capacitor also shows a good high-rate performance, possessing an energy density of 16.62 Wh kg^{-1} at the power density of about 2900 W kg^{-1}.

1. Introduction

Energy storage and conversion devices such as batteries, fuel cells and supercapacitors are attracted extensive consideration in response to ever increasing demands for clean energy technologies. Supercapacitors, known as electrochemical capacitors or ultracapacitors, combining the advantages of dielectric capacitors and rechargeable batteries, can be clarified as: (a) electric double-layer capacitors, which are based on electrochemical charge accumulation at the electric double-layer and (b) redox capacitors or pseudocapacitors, which utilize charge-transfer pseudocapacitance arising from fast and reversible Faradaic reactions occurring at the electrode surface [1–3]. Porous carbon electrodes based on electric double-layer mechanism have been commercially applied in supercapacitors due to their stable physicochemical properties, good conductivity, low cost and long cycling life [4]. On the other side, the capacitance of pseudocapacitor is several times higher than that of the porous carbon [5], but facing the disadvantage of inferior high-rate performance. Although supercapacitors benefit from the high power density, they suffer from a lower energy density than rechargeable batteries. Combining different storage modes in asymmetric capacitors, such as redox/electric double-layer, can make use of the different voltage windows of two electrodes, the high pseudocapacitance, and the high oxygen and/or hydrogen overpotentials of the electrodes, which is beneficial for obtaining high energy density without sacrificing power capability and cycle life [6–9].

In general, hydrous RuO_2 shows the best performance among the metal oxides redox capacitors. However, the high cost of RuO_2 has limited its application in the supercapacitor [10,11]. Therefore, considerable efforts have been made to investigate alternative inexpensive electrode materials with good capacitive characteristics, for example NiO [12], Co_3O_4 [13], MnO_2 [14], $Ni(OH)_2$ [15], $Co(OH)_2$ [16], etc. Correspondingly, improving the capacitive behaviors of these cheap metal oxides/hydroxides is a major step. Since the pseudocapacitance is closely related to the interfacial structure of the material as the electrode, one of the ways to improve the capacitance is to prepare the metal oxide/hydroxide with high surface area, which can provide more active sites for the Faradaic reactions. Recently, there are several techniques developed to synthesize the transition metal oxide/hydroxide, such as electrodeposition [16], chemical precipitation [17], hydrothermal method [18], sol–gel technique [19], and template method [20]. Among them, the template method could be used to prepare the metal oxides with high surface area and ordered structure, but it faces the main disadvantage of complicated process. Ordered mesoporous metal oxides, such as NiO [21], Co_3O_4 [22] and MnO_2 [23], have been synthesized by using ordered mesoporous silica SBA-15 or KIT-6 as the templates. Moreover, a $Co(OH)_2$/Y zeolite nanocomposite was also synthesized using for supercapacitor [24]. Another way for further enhancing the capacitance is to incorporate several metal ions, which can obtain multi-phase metal oxide/hydroxide and introduce abundant structural defects. This approach can also

* Corresponding author. Tel.: +86 21 52412513; fax: +86 21 52413122.
E-mail address: qmgao@mail.sic.ac.cn (Q. Gao).

0378-7753/$ – see front matter © 2009 Elsevier B.V. All rights reserved.
doi:10.1016/j.jpowsour.2009.11.059

improve the stability and cycle life of the metal oxide/hydroxide electrode.

As for the carbon electrode material, current trends include the development of hierarchical structures owing to the high surface area and the pore structures at different size scales [25,26]. Activated carbons with high surface area have been widely adopted as the electrode materials for the supercapacitor, but the pore structures are uncontrollable and the pore sizes are mainly dominated by micropores, which hindered the transportation of the electrolyte ions at high-rate operation [27]. Another approach to produce the porous carbons is carbide-derived-carbon (CDC) technique [28–30]. The CDCs with different mesopore/micropore ratios could be easily controlled by adjusting the synthetic factors. However, chlorinating carbides at high temperature is hazardous. Furthermore, the template technique is recently developed which is used to prepare porous carbon materials as a result of the advantages associated with high surface area and controlled pore structures [31]. Until now, a variety of templates including zeolites [32–34], mesoporous silica or aluminosilicates [35], colloidal particles [36], polymer beads [37], and alumina membranes [38] were used to prepare the porous carbon materials. Although the hierarchical porous carbon could be obtained by applying different templates [37,39], the complicated process limited its industrial application.

Metal-organic frameworks (MOFs) have been developed rapidly in the last decade and they have been used in the fields of gas separation, gas storage and catalysis. It is worth to note that MOF was used as a template to prepare porous carbon material, which provided us a new example of application of the MOF family [40]. In this paper, we study the preparation of hierarchical porous metal oxide/hydroxide and carbon by the template technique. The porous multi-phase Ni–Zn–Co oxide/hydroxide was prepared by using the MOF-5 as the template and nickel and cobalt nitrates as the precursors. The porous carbon was prepared by the direct decomposition of the MOF-5 framework with phenolic resin. The electrochemical properties of the porous Ni–Zn–Co oxide/hydroxide and carbon were investigated. Asymmetric capacitor consisting of a combination of the Ni–Zn–Co oxide/hydroxide as the positive electrode and the porous carbon as the negative electrode was fabricated and its electrochemical performance was studied in detail.

2. Experimental

2.1. Material synthesis

A typical synthesis procedure for MOF-5 could be found in previous report [41]. Briefly, triethylamine (1.6 g) was directly added into a *N*,*N*′-dimethylformamide solution (DMF, 40 mL) containing zinc nitrate (1.21 g) and 1,4-benzenedicarboxylate acid (0.34 g). The solution was strongly stirred at room temperature for 1 h, and then a small amount of H_2O_2 aqueous solution (30 wt%) was added to the above solution. Finally, the white product was filtered, washed with DMF, and finally dried at 100 °C.

The as-prepared MOF-5 was used as a template to prepare the Ni–Zn–Co oxide/hydroxide. Typically, 0.54 g of $Ni(NO_3)_2{\cdot}6H_2O$ and 1.08 g of $Co(NO_3)_2{\cdot}6H_2O$ were dissolved in 20 mL of DMF, followed by addition of 2 g of MOF-5. After stirring at room temperature for at least 24 h, DMF was removed by heating the container at 60 °C. Afterward, the resulting powder was calcined at 300 °C for 5 h in argon atmosphere. Finally, the resultant sample was etched with 4 M NaOH to destroy the MOF-5 framework.

The porous carbon was synthesized as follows. First, a phenolic resin with a low molecular weight was prepared under basic condition [42]. For a typical procedure, 4 mL of formaldehyde solution (37%) was added into 20 mL of water solution containing 2.2 g of phenol, and then 4 g of NaOH was added to the above solution under string. The mixture was heated at 70 °C for 1 h, and the pH was adjusted to 7 by using hydrochloric acid, and then water was vaporized. Then, the obtained phenolic resin was dispersed in 20 mL of DMF and 3.4 g of MOF-5 was added to the above solution. After intensive stirring, DMF was evaporated at 70 °C. Finally, the mixture was carbonized at 200 °C for 2 h, then 600 °C for 4 h and 900 °C for 2 h under nitrogen flow.

2.2. Characterization

The crystal structures of the porous Ni–Zn–Co oxide/hydroxide and carbon materials were characterized by powder X-ray diffraction (XRD) (Rigaku D/MAX-2200) using Ni-filtered Cu Kα radiation (λ = 1.5418 Å). High-resolution transmission electron microscopy (TEM) was carried out using a JEOL JEM-2100F TEM operated at 200 kV. Scanning electron microscopy (SEM) was taken using a JEOL JSM-6700F microscope. Nitrogen adsorption and desorption isotherms were measured at 77 K on a Micrometrics ASAP 2020 system. The specific surface area was calculated using the Brunauer–Emmett–Teller (BET) method in the relative pressure range of 0.02–0.25 for the carbon and 0.05–0.30 for the Ni–Zn–Co oxide/hydroxide. Density functional theory (DFT) software from Micromeritics was used to calculate the pore size distributions (PSDs) from the nitrogen adsorption isotherms.

2.3. Electrochemical evaluation

Electrodes for electrochemical performance were constructed by mixing the prepared active materials, polytetrafluoroethylene and carbon black at a weight ratio of 70:5:25 for the Ni–Zn–Co oxide/hydroxide electrode and 80:10:10 for the carbon electrode in ethanol solutions, and then the mixtures were pressed onto nickel foams at a pressure of 12 MPa. The electrodes were dried at 100 °C overnight and then impregnated with 6 M KOH before electrochemical tests. The electrochemical behaviors of the Ni–Zn–Co oxide/hydroxide and carbon electrodes were characterized by cyclic voltammetry (CV) with a CHI440 electrochemical workstation. The electrochemical measurements were done in a three-electrode experimental setup. The prepared electrode, Pt wire and Ag/AgCl were used as working, counter and reference electrodes, respectively. The capacitance calculated from CV curve is based on the following formula:

$$C_s = \frac{\int IdV}{2\mu m\ \Delta V}$$

where I is the current (A), V is the potential, ΔV is the potential difference during scan, μ is the scan rate, and m is the mass of the active material.

Moreover, asymmetric capacitor using the Ni–Zn–Co oxide/hydroxide as positive electrode and the porous carbon as negative electrode was constructed for cyclic voltammetry and galvanostatic charge–discharge cycling measurements. The weight ratio of the Ni–Zn–Co oxide/hydroxide to carbon is fixed at 1:1. Cyclic voltammograms of asymmetric capacitor were recorded in a two-electrode cell. Galvanostatic charge–discharge cycling was performed using CT2001A (Land, China) at different current densities and the specific gravimetric capacitance of the capacitor was calculated by the equation of

$$C_g = \frac{i\,\Delta t}{\Delta V M}$$

where i is the constant discharging current, Δt is the discharge time, ΔV is the voltage window from the end of the ohmic drop to the end of the discharge process, and M is the mass of the active materials on both positive and negative electrodes.

3. Results and discussion

The XRD pattern of the as-prepared porous Ni–Zn–Co oxide/hydroxide is shown in Fig. 1. The diffraction peaks can be indexed to the metal oxide phase with spinel structure and metal hydroxide. As energy dispersive X-ray spectroscopy (EDS) illustrated (Fig. 2e), the product contains Zn, Ni and Co ions, indicating that the Zn species in MOF-5 involves in the reaction. The metal hydroxide in the Ni–Zn–Co oxide/hydroxide can be clarified as $(Ni,Zn,Co)(OH)_2$. On the other hand, we cannot eliminate the probability of the Ni and Zn ions in the spinel phase, and we speculates that the oxide in the Ni–Zn–Co oxide/hydroxide has the spinel structure with the composition of $(Ni,Zn,Co)Co_2O_4$. The Ni–Zn–Co oxide/hydroxide multi-phase product may contain many structural defects, which can provide more active sites for the redox reactions.

As shown by the TEM image in Fig. 2a, a leaf-like morphology was observed for the obtained Ni–Zn–Co oxide/hydroxide. The electron diffraction pattern taken on a piece of this leaf-like structure reveals a typical crystalline nature (Fig. 2d). High-resolution TEM provided further insight into the nanostructure of the as-prepared Ni–Zn–Co oxide/hydroxide. From Fig. 2b, it is clear to see that the leaf-like sheet contains a lot of nanoparticles with a size of about 5 nm. Furthermore, inspection of Fig. 2c and d indicates that there also exist some layered and amorphous structures. Another point worth mentioning is that the atomic ratio of Ni:Zn:Co measured within the leaf-like structure was determined to be 1:1.129:1.648 from the EDS analysis and the ratio measured outer surface of the particle is 1:2.80:5.026. This result indicates the non-homogeneous distribution of the metal ions, due to the multi-phase character of the obtained Ni–Zn–Co oxide/hydroxide. Fig. 2f shows the representative SEM image of the as-prepared Ni–Zn–Co oxide/hydroxide. It is clear to see that the leaf-like particle agglomerated together and the macropores within the particles ranged in the size of 100–500 nm. On the basis of the analysis results, a probably mechanism of formation of the leaf-like particles is proposed. Due to the microporous characteristic of MOF-5, the metal salt precursors partially fill in the pores of MOF-5 template, resulting in the dispersed nanoparticles. In the process of NaOH treatment, the framework of MOF-5 is destroyed, and the nanoparticles aggregate with each other and form the leaf-like morphology.

The same route was used to prepare the porous carbon. As we know, MOF-5 contains $[O_2C\text{-}C_6H_4\text{-}CO_2]^{2-}$ (1,4-benzenedicarboxylate, BDC) groups. Therefore, the directly decomposition of MOF-5 could synthesize porous carbon material. In our process, the MOF-5 framework was impregnated with phenolic resin before carbonization in order to increase the yield of carbon. From the XRD pattern (Fig. 1), the widen (0 0 2) diffraction peak exhibits that the resultant carbon is low crystalline. SEM image in Fig. 3a reveals that the phenolic resin may not only infiltrate into the pores, but also remain on the outer surfaces of MOF-5. Moreover, there are also macropores between the particles. These macropores can serve as ion-buffering reservoirs, which is essential for the electrochemical activity. As shown by the TEM image in Fig. 3b, the obtained carbon material has disordered pore structure.

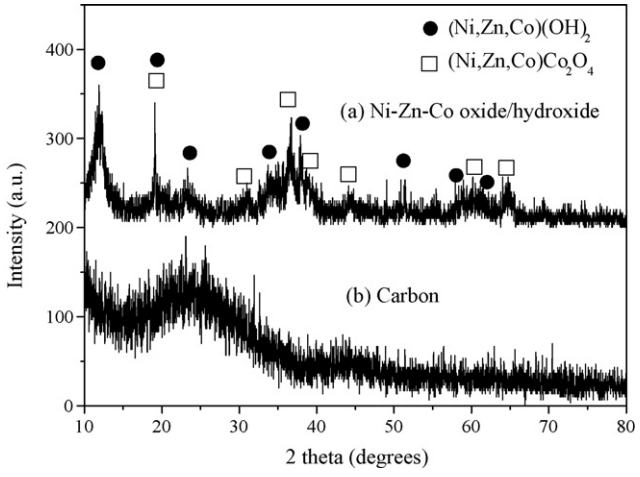

Fig. 1. XRD profiles of the Ni–Zn–Co oxide/hydroxide (a) and carbon (b) electrode materials.

Nitrogen adsorption–desorption isotherms were measured to determine the porosity of the samples (Fig. 4). Type IV isotherms are observed for the porous carbon and Ni–Zn–Co oxide/hydroxide, albeit with marked differences in the adsorption amounts. The steep rise of the initial part of the isotherms for the porous carbon evidences the presence of abundant micropores. However, the negligible amount of nitrogen adsorption for the Ni–Zn–Co oxide/hydroxide at low relative pressure indicates that the micropore contribution is relatively low. With the increase of the relative pressure, both carbon and Ni–Zn–Co oxide/hydroxide have steadily increasing adsorption amounts in the middle-pressure region, which may be attributed to the capillary condensation and multilayer adsorption of nitrogen in the mesopores. And the adsorption curves climb abruptly in the high-pressure region ($>0.8P/P_0$), which are caused by the filling of macropores. The porous carbon shows a surface area of $1614\,m^2\,g^{-1}$ and a pore volume of $2.49\,cm^3\,g^{-1}$, while the surface area and pore volume of the Ni–Zn–Co oxide/hydroxide are $70\,m^2\,g^{-1}$ and $0.20\,cm^3\,g^{-1}$. PSDs obtained by applying the DFT to the nitrogen adsorption data are also shown in Fig. 4. Both samples yielded roughly multimodal PSDs with distinct maxima in the micropore, mesopore and macropore regions, confirming the hierarchical porous structures of the Ni–Zn–Co oxide/hydroxide and carbon materials.

The different electrochemical behaviors of the hierarchical porous carbon and Ni–Zn–Co oxide/hydroxide were compared by means of cyclic voltammetry measurements (Fig. 5). From the rectangular CV curve for the porous carbon electrode (Fig. 5a), it indicates that the capacitive characteristic is a representative electric double-layer capacitance. The corresponding specific capacitance of the carbon electrode calculated from CV curve is $196\,F\,g^{-1}$ at the scan rate of $2\,mV\,s^{-1}$. On one hand, the average value of capacitance per surface area for the carbon electrode is $12.1\,\mu F\,cm^{-2}$, which is comparable to the reported ordered mesoporous carbons and activated carbons ($7–12\,\mu F\,cm^{-2}$) [43]. On the other hand, the capacitance is $157\,F\,g^{-1}$ at $50\,mV\,s^{-1}$ and the capacitance retention ratio at $50\,mV\,s^{-1}$ is 80% with respect to that at $2\,mV\,s^{-1}$. Hence, the carbon electrode with hierarchical porous structure can be favor for fast ion-transport with smaller resistance and rapid charge accumulation, showing the advantage of superior high-rate performance. As for the Ni–Zn–Co oxide/hydroxide, two pairs of redox peaks are visible in the CV curve at $2\,mV\,s^{-1}$ (Fig. 5b), which is distinct from that of the electric double-layer capacitance. And this suggests that the distinct CV behavior mainly results from the redox reactions related to M–O/M–O–OH and M–OH/M–O–OH (M represents metal ions here). The electrochemical capacitance at $2\,mV\,s^{-1}$ is $946\,F\,g^{-1}$ for the Ni–Zn–Co oxide/hydroxide electrode, which is much higher than the samples prepared by using single precursors ($293\,F\,g^{-1}$ for nickel nitrate precursor and $156\,F\,g^{-1}$ for cobalt nitrate precursor). Moreover, the capacitance of Ni–Zn–Co oxide/hydroxide after 50 cycles at $2\,mV\,s^{-1}$ is $941\,F\,g^{-1}$ without obvious capacity fading. The obtained multi-phase metal oxide/hydroxide and the simultaneous presence of Ni, Zn and Co ions may be responsible for its high capacitance and excellent stability. The shape of CV curve of the Ni–Zn–Co oxide/hydroxide changes when the scan rate is increased with only 34% capacitance retention ratio at $20\,mV\,s^{-1}$. The sharp decrease in capacitance is probably due to the diffusion effect of protons within

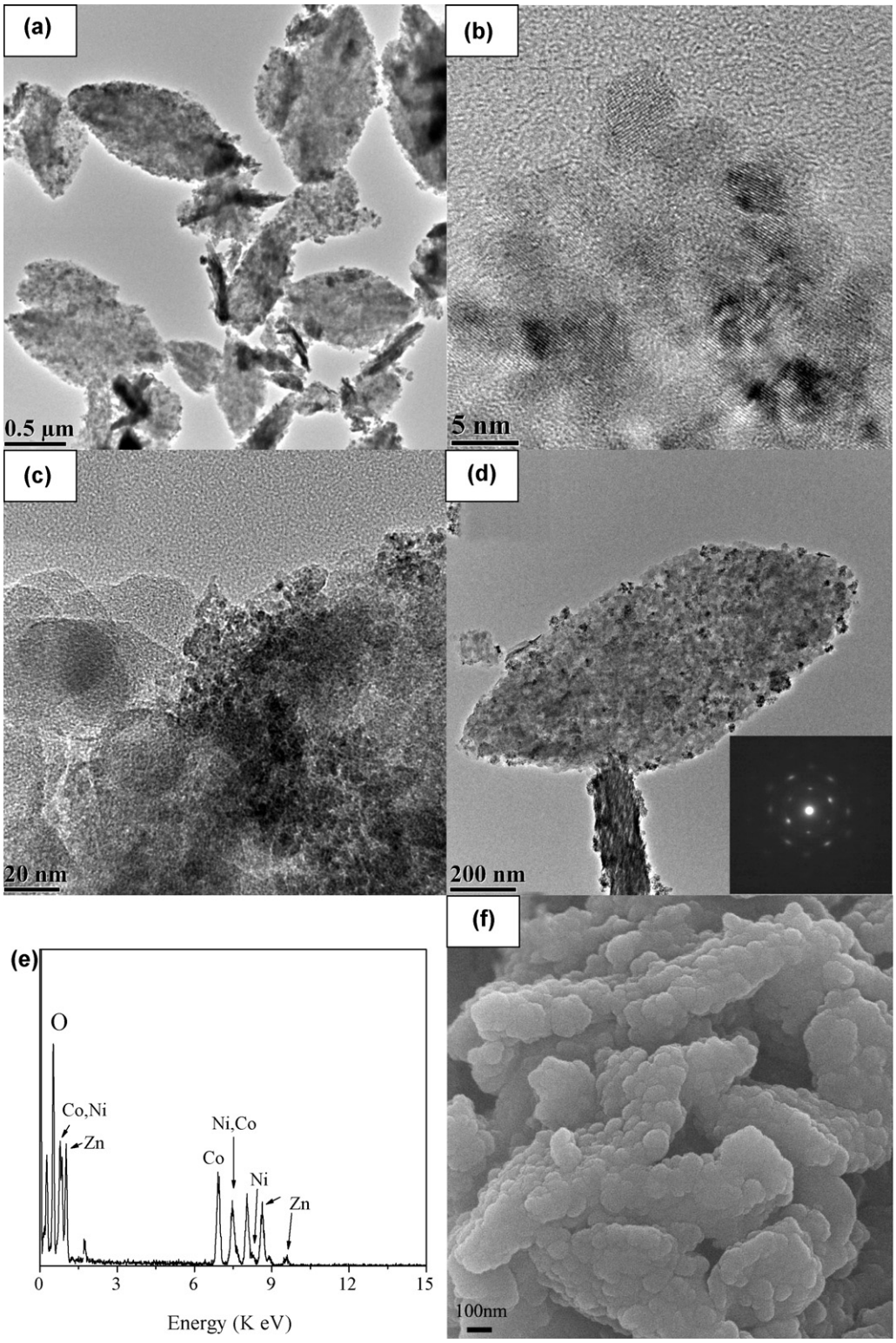

Fig. 2. TEM (a–d), EDS (e) and SEM (f) images of the Ni–Zn–Co oxide/hydroxide.

the electrode and part of the surface of electrode is inaccessible at high scan rate.

Considering the high capacitance of the redox character over the Ni–Zn–Co oxide/hydroxide and the fast ion-transport property of the electric double-layer storage for the carbon, an asymmetric capacitor was assembled using them as the positive and negative electrode, respectively, to evaluate the electrochemical property. Fig. 6a shows the CV curves of the asymmetric capacitor at different operation voltage windows. When the operation voltage window is 1.0 V, the redox humps indicate the pseudocapacitive property. Further increasing the operation voltage window to 1.5 V, more severe Faradaic reactions occurred on the Ni–Zn–Co oxide/hydroxide electrode. Fig. 6b exhibits the CV curves of the asymmetric capacitor operated at 1.5 V at different scan rates. The capacitance at 2 mV s^{-1}

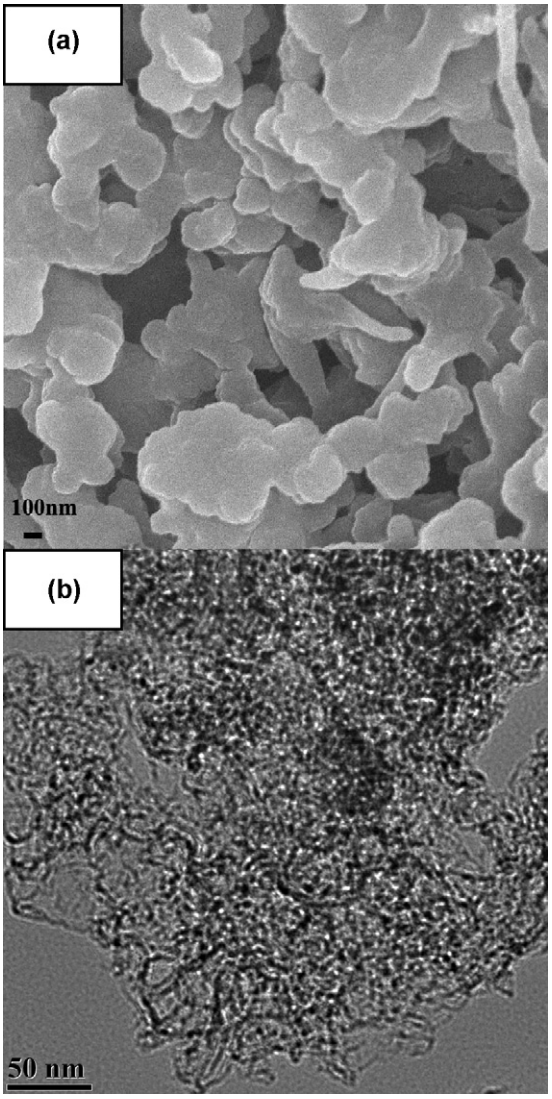

Fig. 3. SEM (a) and TEM images (b) of the as-prepared carbon material.

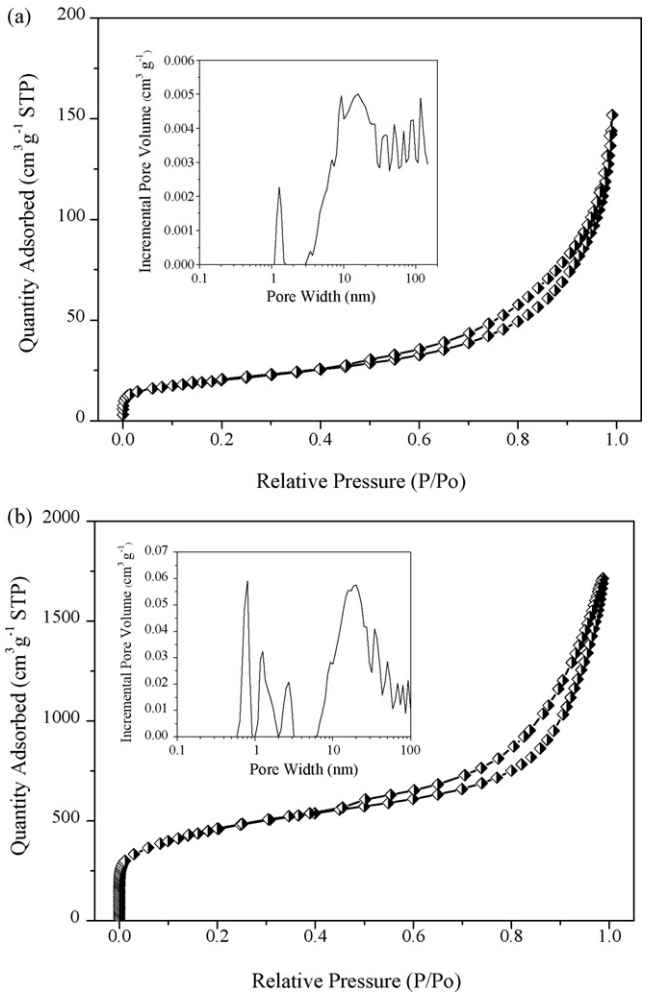

Fig. 4. Nitrogen adsorption–desorption isotherms of the Ni–Zn–Co oxide/hydroxide (a) and carbon material (b). The inset shows the DFT PSDs of the two materials.

is 165 F g^{-1} calculated from the CV curve and the capacitance retention ratio of the asymmetric capacitor operated at 50 mV s^{-1} is 65%. It is clear to see that the capacitance retention ratio of the asymmetric capacitor is superior to the single Ni–Zn–Co oxide/hydroxide electrode.

The applicability of asymmetric capacitors can also be evaluated by means of galvanostatic charging–discharging method. Fig. 7 shows the variation of specific gravimetric capacitance with the increase of the current density at different operation voltage windows. At 0.25 A g^{-1}, the specific capacitance is 69 F g^{-1} operated at 1.0 V, while the value is 37 F g^{-1} at the current density of 10 A g^{-1}. The capacitance retention ratio at 10 A g^{-1} is 54% with respect to that at 0.25 A g^{-1}. When the operation voltage window is 1.3 V, the capacitance at 0.25 and 10 A g^{-1} is 84 and 58 F g^{-1}, respectively, cor-

Table 1
Comparison of the energy density of the asymmetric capacitors[a].

Positive electrodes	Negative electrodes	Electrolytes	Operation voltages (V)	Energy densities (Wh kg^{-1})	Refs.
Ni–Zn–Co oxide/hydroxide	Porous carbon	6 M KOH	0–1.5	41.65	This work
OMC	Titania NT	1 M $LiPF_6$	0–3.0	42	[7]
$Ni(OH)_2$ + carbon NT	AC	6 M KOH	0–1.5	40	[8]
MnO_2	AC	0.5 M K_2SO_4	0–1.8	28.4	[9]
LMO	LTPO	1 M Li_2SO_4	0–1.85	60	[44]
Carbon NT	Titania NW	1 M $LiPF_6$	0–2.8	12.5	[45]
MnO_2	AC	0.65 M K_2SO_4	0–2.2	19	[46]
NiO	Porous carbon	6 M KOH	0–1.5	~13	[47]
LMO + AC	LTO	1 M $LiPF_6$	1.2–2.8	16.47	[48]
MnO_2	AC	2 M KNO_3	0–2.0	21.0	[49]
Fe_3O_4	AC	6 M KOH	0–1.2	~7.6[b]	[50]
$V_2O_5{\cdot}0.6H_2O$	AC	0.5 M K_2SO_4	0–1.8	29.0	[51]

[a] Nanotube, nanowire, activated carbon and ordered mesoporous carbon were denoted as NT, NW, AC and OMC, respectively. LMO, LTO and LTPO represented as $LiMn_2O_4$, $Li_4Ti_5O_{12}$ and $LiTi_2(PO_4)_3$, respectively.
[b] Energy density not provided in the publication but calculated from the capacitance and operation voltage window.

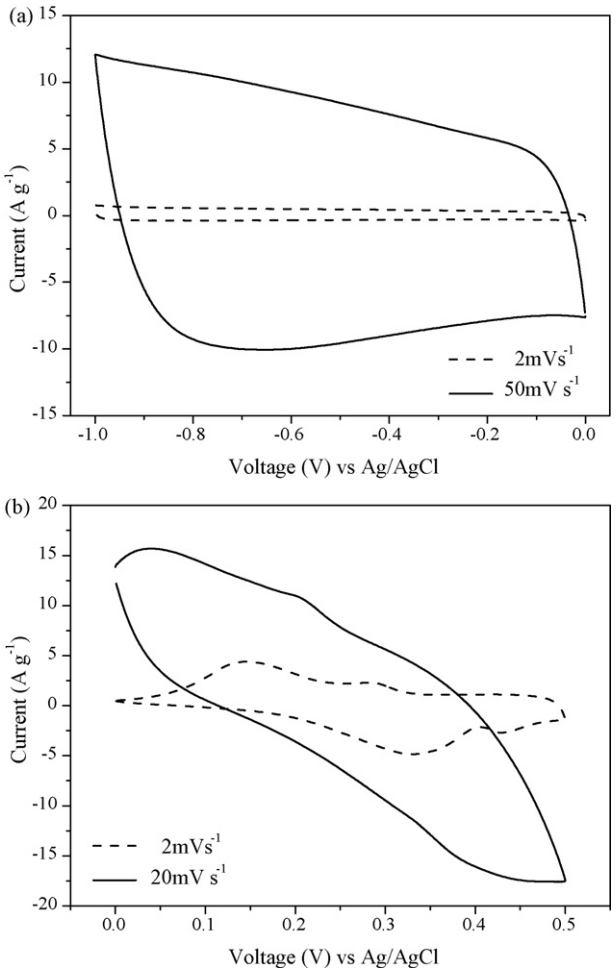

Fig. 5. CV profiles of the carbon (a) and Ni–Zn–Co oxide/hydroxide (b) at different scan rates.

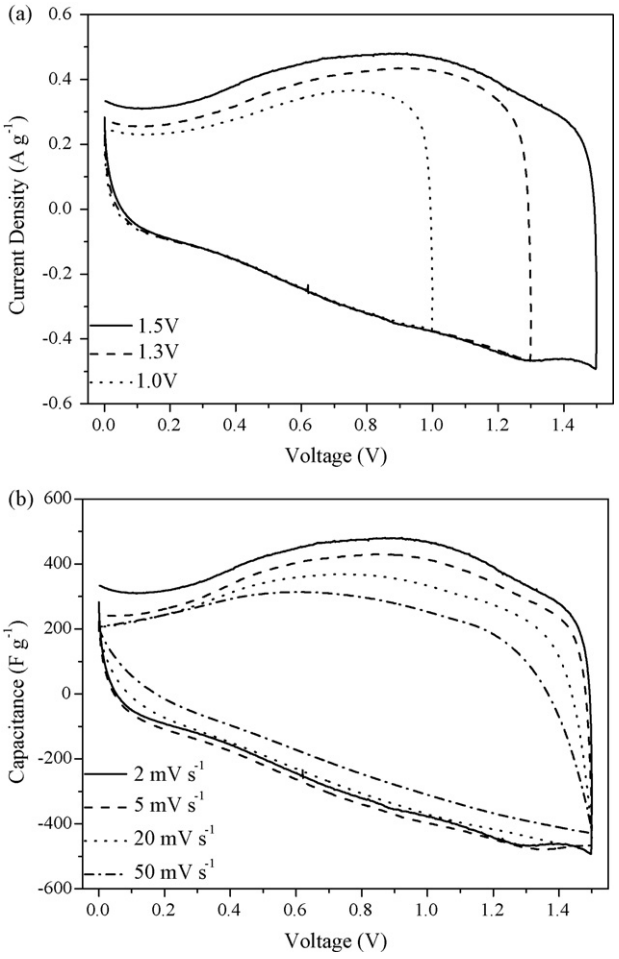

Fig. 6. CV curves of the asymmetric capacitor with different operation voltage windows recorded at 2 mV s^{-1} (a) and CV profiles of the asymmetric capacitor (operated at 1.5 V) measured from 2 to 50 mV s^{-1} (b).

responding to a capacitance retention ratio of 69%. Moreover, the high capacitance is 136 F g^{-1} operated at 1.5 V and 0.25 A g^{-1}, and the value is 89 F g^{-1} at 10 A g^{-1} with a 65% retention ratio. It is noteworthy that the specific gravimetric capacitance and capacitance retention ratio were enhanced to a certain degree by increasing the operation voltage window due to the pseudocapacitive contribution.

The Ragone plots in Fig. 8, which correlate the energy density with power density, were calculated from the galvanostatic charging–discharging plots. It is obvious that both the energy density and power density are remarkably enhanced upon raising the operation voltage. The highest energy density operated at 1.5 V is 41.65 Wh kg^{-1}, which is about double or four times that operated at 1.3 or 1.0 V. Such a high energy density is comparable to or even higher than other asymmetric capacitors using organic or aqueous electrolytes (Table 1). The aqueous electrolyte applied here exhibits several advantages than organic electrolyte associated with its low cost, high conductivity, high safety and environmental benign character [44]. Remarkably, the asymmetric capacitor operated at 1.5 V is capable of delivering a high energy density of 16.62 Wh kg^{-1} and a high power density of about 2900 W kg^{-1} at the current density of 10 A g^{-1}.

Cycling performance of asymmetric capacitors at different operation voltage windows was evaluated at 2 A g^{-1} for 1000 cycles. Fig. 9a shows the galvanostatic charging–discharging profiles at the 1st and 1000th cycles of the asymmetric capacitor. Obviously, the discharging time slightly increased after 1000 cycles at the operation voltage windows of 1.0 and 1.3 V, showing the excellent cycling stability. On the other hand, the discharging time decreased after 1000 cycles at the operation voltage window of 1.5 V, which is caused by certain irreversible Faradaic reactions. Fig. 9b displays the variations in energy density as a function of cycle number. The trend of asymmetric capacitor operated at 1.0 and 1.3 V in

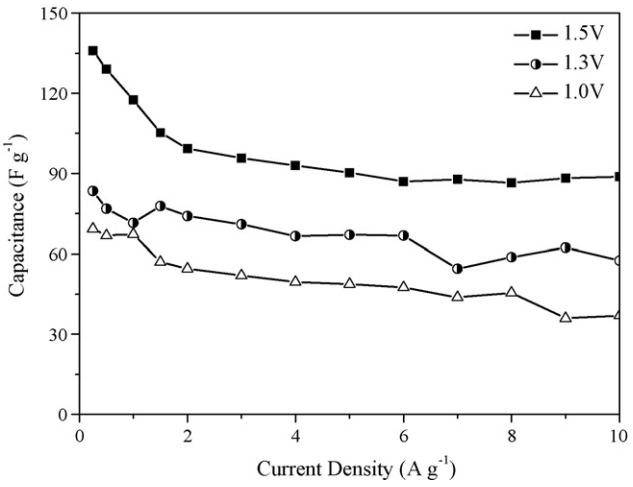

Fig. 7. Variation of the capacitance of the asymmetric capacitor operated at different voltage windows with the increase of current density.

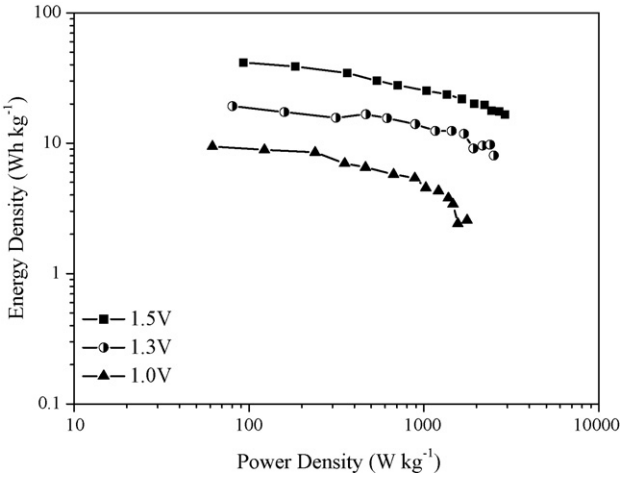

Fig. 8. Ragone plots of power density versus energy density for the asymmetric capacitor with different operation voltage windows.

energy-density variations with cycle war similar, which displayed a slightly increase along with the cycling proceeded. On the other hand, the asymmetric capacitor operated at 1.5 V exhibited about 16% energy-density decay after 1000 cycles.

The excellent electrochemical performance of the asymmetric capacitor can be reasonably ascribed to the synergistic effect between the positive and negative electrodes. First, the porous carbon with hierarchical structure and high surface area tends to facilitate ion-transportation rate and increase the charge capacity. Besides, the hierarchical carbon electrode in the asymmetric capacitor is favorable for keeping a high power density and a long cycle life. Second, the multi-phase metal oxide/hydroxide can provide more active sites for the redox reactions, resulting in a large pseudocapacitance. Moreover, the energy density of the asymmetric capacitor is significantly enhanced due to the higher capacitance and operation voltage. Consequently, the utilization of redox and electric double-layer electrodes for the asymmetric capacitor can be beneficial for obtaining high energy density without obvious sacrificing power capability and cycle life.

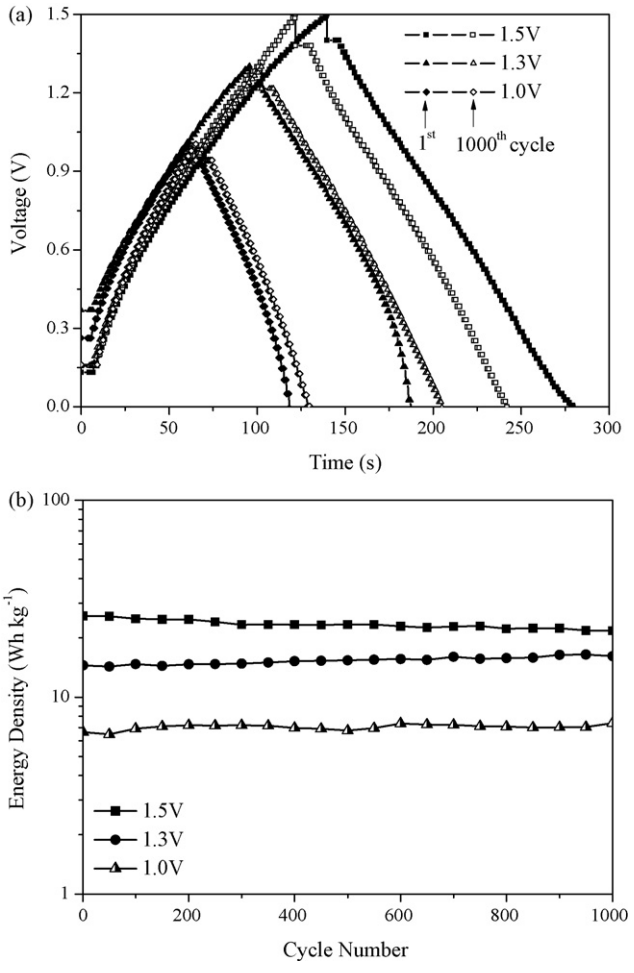

Fig. 9. Galvanostatic charging–discharging profiles at 1st and 1000th cycles (a), and variation of the energy density as a function of cycle number (b).

4. Conclusions

In this paper, hierarchical porous carbon and Ni–Zn–Co oxide/hydroxide were prepared by the template method using MOF-5 as the template. The carbon material with the hierarchical structure exhibits a superior high-rate performance. And the Ni–Zn–Co oxide/hydroxide electrode shows a large pseudocapacitance due to the multi-phase character and the simultaneous presence of Ni, Zn and Co ions. An asymmetric capacitor is assembled using the Ni–Zn–Co oxide/hydroxide as the positive electrode and the porous carbon as the negative electrode. The asymmetric capacitor can deliver an energy density of 41.65 Wh kg^{-1} and the high-rate performance is improved which is superior to the single metal oxide/hydroxide. A good rate behavior with the energy density of 16.62 Wh kg^{-1} at the power density of about 2900 W kg^{-1} can be obtained. Moreover, the assembled asymmetric capacitor shows rather good cycling behaviors. The asymmetric capacitor operated at 1.5 V showed about 16% energy-density decay after 1000 cycles due to certain irreversible redox reactions. Thus, combining redox and electric double-layer storage modes in this asymmetric capacitor can inherit the advantages of the two different storage mechanisms, showing a high energy density without obvious sacrificing the high power density and long cycle life.

Acknowledgments

We thank the Chinese National Science Foundation (No. U0734002), Shanghai Basic Key Program (No. 09JC1415100) and Shanghai Nanotechnology Promotion Center (No. 0852nm0500) for the financial supports.

References

[1] B.E. Conway, Electrochemical Supercapacitors: Scientific Fundamentals and Technological Applications, Plenum Publishers, New York, 1999, pp. 1–220.
[2] P. Simon, Y. Gogosti, Nat. Mater. 7 (2008) 845–854.
[3] E. Frackowiak, F. Béguin, Carbon 39 (2001) 937–950.
[4] A.G. Pandolfo, A.F. Hollenkamp, J. Power Sources 157 (2006) 11–27.
[5] J.P. Zheng, P.J. Cygan, T.R. Jow, J. Electrochem. Soc. 142 (1995) 2699–2703.
[6] J. Li, F. Gao, J. Power Sources 194 (2009) 1184–1193.
[7] D.W. Wang, H.T. Fang, F. Li, Z.G. Chen, Q.S. Zhong, G.Q. Lu, H.M. Cheng, Adv. Funct. Mater. 18 (2008) 3787–3793.
[8] Y.G. Wang, L. Yu, Y.Y. Xia, J. Electrochem. Soc. 153 (2006) A743–A748.
[9] Q. Qu, P. Zhang, B. Wang, Y. Chen, S. Tian, Y. Wu, R. Holze, J. Phys. Chem. C 113 (2009) 14020–14027.
[10] Y.F. Ke, D.S. Tsai, Y.S. Huang, J. Mater. Chem. 15 (2005) 2122–2127.
[11] T. Cottineau, M. Toupin, T. Delahaye, T. Brousse, D. Bélanger, Appl. Phys. A 82 (2006) 599–606.
[12] J.W. Lang, L.B. Kong, W.J. Wu, Y.C. Luo, L. Kang, Chem. Commun. (2008) 4213–4215.
[13] M.B. Zheng, J. Cao, S.T. Liao, J.S. Liu, H.Q. Chen, Y. Zhao, W.J. Dai, G.B. Ji, J.M. Cao, J. Tao, J. Phys. Chem. C 113 (2009) 3887–3894.
[14] A.E. Fisher, K.A. Pettigrew, D.R. Rolison, R.M. Stround, J.W. Long, Nano Lett. 7 (2007) 281–286.
[15] U.M. Patil, K.V. Gurav, V.J. Fulari, C.D. Lokhande, O.S. Joo, J. Power Sources 188 (2009) 338–342.
[16] W.J. Zhou, J. Zhang, T. Xue, D.D. Zhao, H.L. Li, J. Mater. Chem. 18 (2008) 905–910.
[17] Q.S. Song, Y.Y. Li, S.L.I. Chan, J. Appl. Electrochem. 35 (2005) 157–162.
[18] L. Dong, Y. Chu, W. Sun, Chem. Eur. J. 14 (2008) 5064–5072.

[19] J. Cheng, G.P. Cao, Y.S. Yang, J. Power Sources 159 (2006) 734–741.
[20] B.Z. Tian, X.Y. Liu, L.A. Solovyov, Z. Liu, H.F. Yang, Z.D. Zhang, S.H. Xie, F.Q. Zhang, B. Tu, C.Z. Yu, O. Terasaki, D.Y. Zhao, J. Am. Chem. Soc. 126 (2004) 865–875.
[21] F. Jiao, A.H. Hill, A. Harrison, A. Berko, A.V. Chadwick, P.G. Bruce, J. Am. Chem. Soc. 130 (2008) 5262–5266.
[22] A. Rumplecker, F. Kleitz, E.L. Salabas, F. Schüth, Chem. Mater. 19 (2007) 485–496.
[23] F. Jiao, P.G. Bruce, Adv. Mater. 19 (2007) 657–660.
[24] L. Cao, F. Xu, Y.Y. Liang, H.L. Li, Adv. Mater. 16 (2004) 1853–1856.
[25] J. Huang, B.G. Sumpter, V. Meunier, Chem. Eur. J. 14 (2008) 6614–6626.
[26] D.W. Wang, F. Li, M. Liu, G.Q. Lu, H.M. Cheng, Angew. Chem. Int. Ed. 47 (2008) 373–376.
[27] K. Xia, Q. Gao, J. Jiang, J. Hu, Carbon 46 (2008) 1718–1726.
[28] C. Largeot, C. Portet, J. Chmiola, P.L. Taberna, Y. Gogosti, P. Simon, J. Am. Chem. Soc. 130 (2008) 2730–2731.
[29] J. Leis, M. Arulepp, A. Kuura, M. Lätt, E. Lust, Carbon 44 (2006) 2122–2129.
[30] H. Wang, Q. Gao, Carbon 47 (2009) 820–828.
[31] C.O. Ania, V. Khomenko, E. Raymundo-Piñero, J.B. Parra, F. Béguin, Adv. Funct. Mater. 17 (2007) 1828–1836.
[32] Z. Ma, T. Kyotani, A. Tomita, Carbon 40 (2002) 2367–2374.
[33] Z. Yang, Y. Xia, R. Mokaya, J. Am. Chem. Soc. 129 (2007) 1673–1679.
[34] H. Wang, Q. Gao, J. Hu, Z. Chen, Carbon 47 (2009) 2259–2268.
[35] Y. Xia, R. Mokaya, Adv. Mater. 16 (2004) 886–891.
[36] H. Yamada, H. Nakamura, F. Nakahara, I. Moriguchi, T. Kudo, J. Phys. Chem. C 111 (2007) 227–233.
[37] S.W. Woo, K. Dokko, H. Nakano, K. Kanamura, J. Mater. Chem. 18 (2008) 1674–1680.
[38] K. Wang, Y. Wang, Y. Wang, E. Hosono, H. Zhou, J. Phys. Chem. C 113 (2009) 1093–1097.
[39] H.I. Lee, C. Pak, C.H. Shin, H. Chang, D. Seung, J.E. Yie, J.M. Kim, Chem. Commun. (2005) 6035–6037.
[40] B. Liu, H. Shioyama, T. Akita, Q. Xu, J. Am. Chem. Soc. 130 (2008) 5390–5391.
[41] L. Huang, H. Wang, J. Chen, Z. Wang, J. Sun, D. Zhao, Y. Yan, Micropor. Mesopor. Mater. 58 (2003) 105–114.
[42] C. Xue, B. Tu, D. Zhao, Adv. Funct. Mater. 18 (2008) 3914–3921.
[43] E. Frackowiak, Phys. Chem. Chem. Phys. 9 (2007) 1774–1785.
[44] J.Y. Luo, Y.Y. Xia, Adv. Funct. Mater. 17 (2007) 3877–3884.
[45] Q. Wang, Z. Wen, J. Li, Adv. Funct. Mater. 16 (2006) 2141–2146.
[46] V. Khomenko, E. Raymundo-Piñero, F. Béguin, J. Power Sources 153 (2006) 183–190.
[47] D.W. Wang, F. Li, H.M. Cheng, J. Power Sources 185 (2008) 1563–1568.
[48] X. Hu, Z. Deng, J. Suo, Z. Pan, J. Power Sources 187 (2009) 635–639.
[49] T. Brousse, M. Toupin, D. Bélanger, J. Electrochem. Soc. 151 (2004) A614–A622.
[50] X. Du, C. Wang, M. Chen, Y. Jiao, J. Wang, J. Phys. Chem. C 113 (2009) 2643–2646.
[51] Q.T. Qu, Y. Shi, L.L. Li, W.L. Guo, Y.P. Wu, H.P. Zhang, S.Y. Guan, R. Holze, Electrochem. Commun. 11 (2009) 1325–1328.